


Active shape control by plants in dynamic environmentsHadrien Oliveri ^{1,2,3,4} Derek E. Moulton ¹ Heather A. Harrington ^{1,2,3,4} and Alain Goriely ^{1,*}¹*Mathematical Institute, University of Oxford, Oxford OX2 6GG, United Kingdom*²*Max-Planck-Institut für molekulare Zellbiologie und Genetik, Dresden 01307, Germany*³*Center for Systems Biology Dresden, Dresden 01307, Germany*⁴*Fakultät Mathematik, Technische Universität Dresden, Dresden 01062, Germany* (Received 14 September 2023; revised 30 January 2024; accepted 6 May 2024; published 12 July 2024)

Plants are a paradigm for active shape control in response to stimuli. For instance, it is well known that a tilted plant will eventually straighten vertically, demonstrating the influence of both an external stimulus, gravity, and an internal stimulus, proprioception. These effects can be modulated when a potted plant is additionally rotated along the plant's axis, as in a rotating clinostat, leading to intricate shapes. We use a previously derived rod model to study the response of a growing plant and the joint effects of both stimuli at all rotation speeds. In the absence of rotation, we identify a universal planar shape towards which all shoots eventually converge. With rotation, we demonstrate the existence of a stable family of three-dimensional dynamic equilibria where the plant axis is fixed in space. Further, the effect of axial growth is to induce steady behaviors, such as solitary waves. Overall, this study offers insight into the complex out-of-equilibrium dynamics of a plant in three dimensions and further establishes that internal stimuli in active materials are key for robust shape control.

DOI: [10.1103/PhysRevE.110.014405](https://doi.org/10.1103/PhysRevE.110.014405)**I. INTRODUCTION**

Active materials are characterized by their ability to adapt to external stimuli, often manifested by changes in shape. A paradigm of this adaptability is observed in the growth patterns of plant shoots, which exhibit remarkable sensitivity not only to their environment (e.g., light, gravity, wind) [1] but also, intriguingly, to their own evolving shapes, a phenomenon called *proprioception* [2,3]. We show that this synergistic response to multiple stimuli serves as a robust mechanism for plants to maintain their shape in highly dynamic environments. An important type of response in plant shoots is *gravitropism* [Fig. 1(a)], the tendency to react and orient their growth against the direction of gravity [4]. While modifying gravity experimentally is challenging, it is possible to nullify its influence by rotating the plant sufficiently fast in a *clinostat* [5], shown in Fig. 1(b). This device, patented by Julius von Sachs circa 1880 [6,7], imparts a constant rotational motion to the plant, thereby cyclically altering the relative direction of gravity. To simulate weightlessness, the clinostat must rotate at a relatively high angular speed ω , compared to the response of the plant, allowing for the averaging out of gravity's influence over multiple rotations [8]. In such a case, the plant grows straight. Further, the general observation that growing shoots tend to straighten in the absence of

other influences indicates another well-established necessary response, called *autotropism*, the tendency to minimize curvature during growth [9]. Under slower rotations, the relative influence of autotropism and gravitropism can be gauged by varying the angular speed, leading to the possibility of complex three-dimensional shapes that we study here.

The first model for the gravitropic response of slender shoots was formulated by Sachs in 1879 [7]. His *sine law* states that the rate of change of curvature at a point is given by the sine of the inclination angle $\theta(s, t)$ between the tangent to the shoot centerline and the vertical direction, where s is the arclength from the base and t is time [Fig. 1(a)]. Recalling that the curvature is the arclength derivative of this angle, the sine law can be expressed as

$$\dot{\theta}' + \alpha \sin \theta = 0, \quad (1)$$

with α a rate constant and where $(\cdot)'$ and $(\dot{\cdot})$ denote differentiation w.r.t. s and t , respectively. Notably, unbeknownst to Sachs and his successors, the sine law is an instance of the celebrated sine-Gordon equation, a fully integrable system with a well-known conservative structure [10]; in fact, the sine law is the earliest appearance of this equation as a physical model. While the sine law is the starting point of many augmented models [9,11–17], it is restricted to planar motion and does not include autotropism, which is necessary for shoots to eventually straighten [9,18].

Here we follow the plant tropism modeling framework developed in [1] to model the clinostatting plant in three dimensions as an unshearable and inextensible *morphoelastic rod* [20,21] of length ℓ . We neglect self-weight and centrifugal effects, which is valid for small shoots and slow rotation (i.e., $\rho g \ell^3 \ll B$ and $\rho \omega^2 \ell^4 \ll B$, with B and ρ denoting the bending

*Contact author: goriely@maths.ox.ac.uk

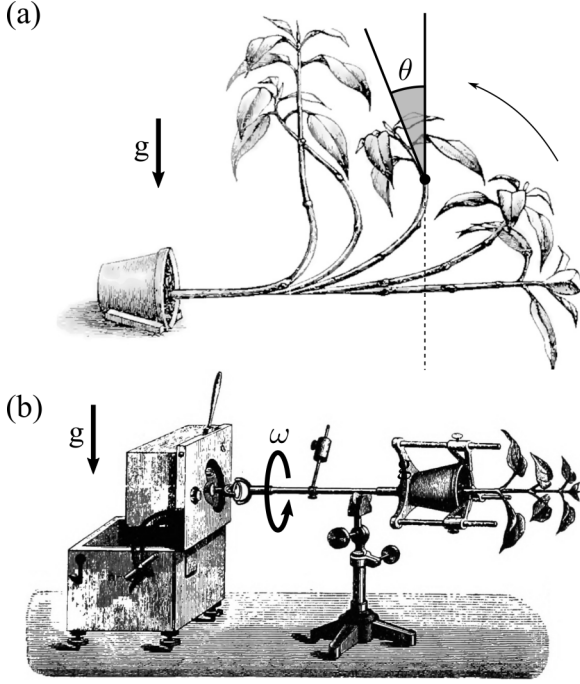


FIG. 1. (a) A potted plant realigns itself with gravity when tilted horizontally. (b) In a clinostat, the effect of gravity is nullified at sufficient angular speed. In both cases the plant's axis lies in a plane. (Adapted from [19].)

stiffness and the linear density, respectively). In this case, the shoot assumes its stress-free shape. While the intrinsic shape is the result of a balance of internal elastic stresses due to growth, we assume that the extra stresses acting on the centerline are negligible. In the first scenario studied here, we also neglect the axial growth of the shoot and focus on curvature generation through tissue growth and remodeling. Thus, the shoot has a constant length (we address elongation at a later stage).

II. MODEL

The centerline of a rod is a spatial curve $\mathbf{r}(s, t) = x(s, t)\mathbf{i} + y(s, t)\mathbf{j} + z(s, t)\mathbf{k}$, parametrized here by its arclength $s \in [0, \ell]$ ($s = 0$ at the base) at time $t \geq 0$; where $\{\mathbf{i}, \mathbf{j}, \mathbf{k}\}$ is the canonical basis of \mathbb{R}^3 , with \mathbf{k} pointing upward against the gravity direction (Fig. 2). The Frenet-Serret frame $\{\mathbf{t}, \mathbf{n}, \mathbf{b}\}$, is built from the tangent vector $\mathbf{t} := \mathbf{r}'$ and the unit normal and binormal vectors, \mathbf{n} and \mathbf{b} , defined through

$$\mathbf{t}' = \kappa \mathbf{n}, \quad \mathbf{n}' = \tau \mathbf{b} - \kappa \mathbf{t}, \quad \mathbf{b}' = -\tau \mathbf{n}, \quad (2)$$

where κ and τ are the curvature and torsion, respectively. In addition to its centerline, a rod is equipped with a right-handed orthonormal director basis $\mathbf{d}_1(s, t)$, $\mathbf{d}_2(s, t)$, and $\mathbf{d}_3(s, t) = \mathbf{t}(s, t)$ [21] that obeys

$$\mathbf{d}_i' = \mathbf{u} \times \mathbf{d}_i, \quad \mathbf{d}_i' = \mathbf{w} \times \mathbf{d}_i, \quad i = 1, 2, 3. \quad (3)$$

The Darboux vector \mathbf{u} and spin vector \mathbf{w} obey the compatibility condition

$$\dot{\mathbf{u}} - \mathbf{w}' = \mathbf{w} \times \mathbf{u}. \quad (4)$$

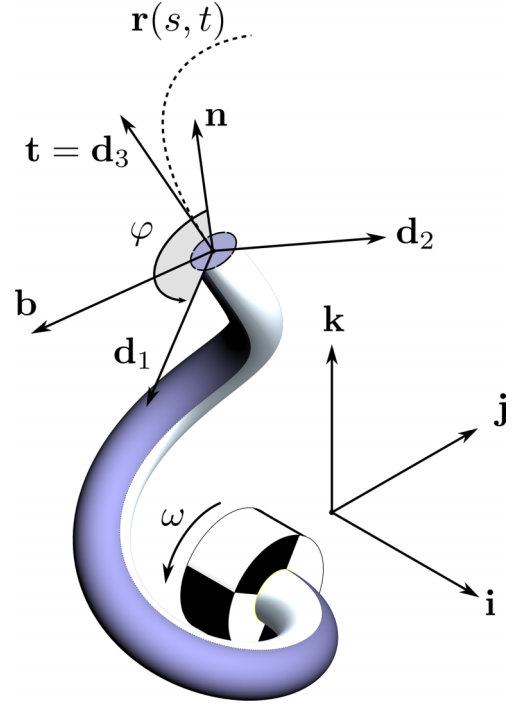


FIG. 2. Rod model for a clinostatting plant. We model the shoot as a rod with centerline \mathbf{r} and tangent $\mathbf{t} = \mathbf{d}_3$. At a given point at arclength s from the base, the vectors \mathbf{d}_1 and \mathbf{d}_2 lie in the principal directions of the cross section. At the base of the rod, \mathbf{d}_1 and \mathbf{d}_2 are rotating around \mathbf{i} with angular speed ω .

The evolution of the tangent vector along the shoot is given by Eq. (3):

$$\mathbf{t}' = \mathbf{u} \times \mathbf{t}. \quad (5)$$

In gravitropism, gravisensing mechanisms activate pathways that result in differential growth of the cells [2,15,22–27]. Changes in curvature then occur when cells on the bottom side of the shoot expand more than those on the upper side [1,25,28], a phenomenon reminiscent of, and mechanically equivalent to, the thermal bending of a bimetallic strip [29]. As shown in [1], assuming local growth laws for both gravitropism and autotropism leads, through dimensional reduction [30], to a generalization of the sine law that includes autotropism and three-dimensional effects, written as (Appendix A):

$$\dot{\mathbf{u}} + \mathbf{u} \times \mathbf{w} = \alpha \mathbf{t} \times \mathbf{k} - \beta \mathbf{u}. \quad (6)$$

Here $\mathbf{u} \times \mathbf{w}$ accounts for the passive advection of \mathbf{u} by the spin vector \mathbf{w} . The first term in the r.h.s accounts for gravitropism with rate constant α . The second term models autotropism, with rate constant β , and leads to an exponential decay in time of the curvature in the absence of other effects. This equation reduces to the sine law in the planar case when $\beta = 0$ and no rotation is imposed. The relative strength of gravitropism and autotropism is captured by the dimensionless *bending number* $\lambda := \alpha \ell / \beta$ [9,13]. The constitutive hypothesis that the local growth of the cells is parallel to the central axis precludes the rod from twisting, imposing [30]

$$\mathbf{u} \cdot \mathbf{t} = 0. \quad (7)$$

Geometrically, a consequence is that \mathbf{d}_1 and \mathbf{d}_2 propagate parallel to the curve, i.e., the field of directors $\{\mathbf{d}_1, \mathbf{d}_2, \mathbf{d}_3\}$ forms a so-called *Bishop frame* [31]. For such a rod, the following identities hold [21]:

$$\kappa = \sqrt{\mathbf{u} \cdot \mathbf{u}}, \quad \tau = -\frac{\partial}{\partial s} \arctan\left(\frac{\mathbf{d}_1 \cdot \mathbf{u}}{\mathbf{d}_2 \cdot \mathbf{u}}\right). \quad (8)$$

The torsion τ here measures the winding rate of the curvature vector \mathbf{u} around the centerline as we move along the rod.

Equations (4)–(7) form a closed system for \mathbf{u} , \mathbf{w} , and \mathbf{t} which, given appropriate initial and boundary conditions, fully captures the shape and evolution of the shoot. For comparison, our model is the *three-dimensional* and geometrically exact generalization of the standard “AC model,” which has been validated experimentally in numerous genera [9]. In particular, our approach is general enough to include complex movements such as clinostatting, enforced through a nonzero spin $\mathbf{w}(0, t) \neq \mathbf{0}$ at the base.

III. EQUILIBRIA

We start our analysis by looking for equilibrium solutions in the absence of rotation, but for an arbitrary orientation of the base θ_0 (Appendix B). In that case the equilibrium solution is planar with the exact solution $\tilde{z}\lambda/\ell = \log(\sin\theta_0) - \log[\sin(\theta_0 - \tilde{x}\lambda/\ell)]$, for $0 \leq \tilde{x}\lambda/\ell < \theta_0$, with the tilde denoting quantities at equilibrium. We will establish that this solution is stable and gives the asymptotic shape of the shoot centerline when the base is tilted to an angle θ_0 from the vertical, as shown in Fig. 3(a). On rescaling all lengths by the *auto-gravitropic length* $\ell_{ag} := \ell/\lambda$, we obtain a universal curve [see Fig. 3(b)]:

$$\tilde{z} = \log(\sin\theta_0) - \log[\sin(\theta_0 - \tilde{x})], \quad 0 \leq \tilde{x} < \theta_0. \quad (9)$$

We refer to this curve as the *simple caulinoïd* (from Latin *caulis*, meaning stem).

Next, we consider a clinostat imparting a counterclockwise rotation around the horizontal axis \mathbf{i} with period $T = 2\pi/\omega$. In this case the boundary conditions are $\mathbf{t}(0, t) = \mathbf{i}$ and $\mathbf{w}(0, t) = \omega\mathbf{i}$. By definition, at equilibrium, we have $\dot{\mathbf{w}} = \dot{\mathbf{u}} = \dot{\mathbf{t}} = \mathbf{0}$, which gives $\mathbf{w} = \omega\mathbf{t}$. In this configuration, the shoot revolves at constant angular velocity ω about a *fixed* centerline [Fig. 3(a)] with tangent vector given by (Appendix B)

$$\tilde{\mathbf{t}}(s) = \frac{\cos \Lambda s}{\cosh \Theta s} \mathbf{i} - \frac{\sin \Lambda s}{\cosh \Theta s} \mathbf{j} + \tanh(\Theta s) \mathbf{k}, \quad (10)$$

where $\Lambda := \alpha\omega/(\omega^2 + \beta^2)$ and $\Theta := \alpha\beta/(\omega^2 + \beta^2)$. The curvature, $\tilde{\kappa}(s) = \sqrt{\Theta^2 + \Lambda^2} \operatorname{sech} \Theta s$, and torsion, $\tilde{\tau}(s) = -\Lambda \tanh \Theta s$, of this general caulinoïd satisfy

$$\frac{\tilde{\kappa}^2}{\Theta^2 + \Lambda^2} + \frac{\tilde{\tau}^2}{\Lambda^2} = 1. \quad (11)$$

Thus, along an equilibrium solution, starting from $\tilde{\tau}(0) = 0$ at the base, the torsion increases while the curvature decreases along an ellipse in the curvature-torsion plane. In physical space, the centerline follows a modulated left-handed helix that gradually uncoils away from the base towards the vertical, and we can interpret Λ and Θ as the curve’s *winding* and *rise* densities [Fig. 4(b)]. In the limit $\omega \rightarrow 0$, we have $\Lambda = 0$ and $\Theta = 1/\ell_{ag}$, recovering the planar case discussed above.

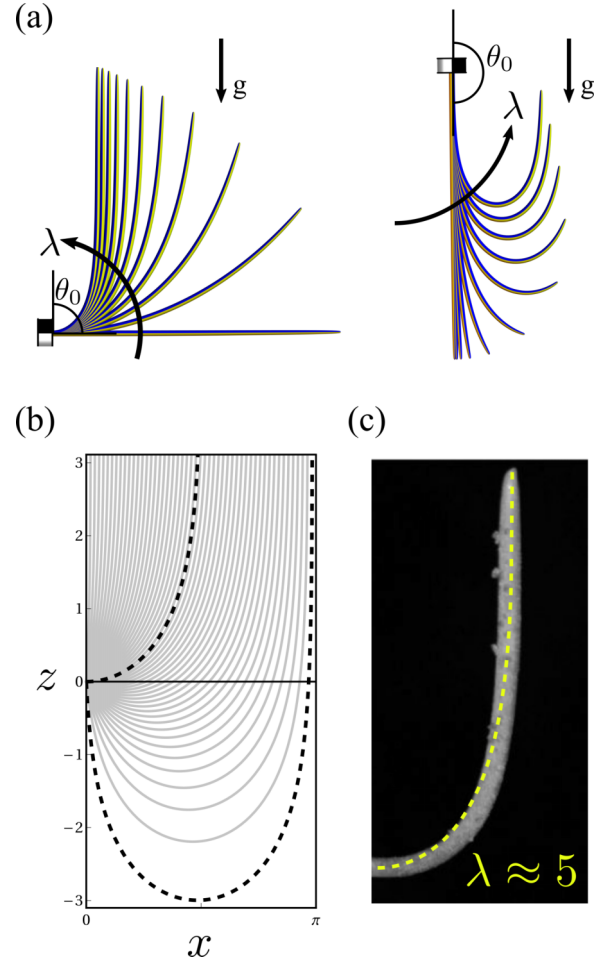


FIG. 3. Steady solutions in the absence of clinostatting. (a) Horizontal clamp $|\theta_0| = \pi/2$ and upside-down clamp $|\theta_0| \rightarrow \pi^-$ for various λ . (b) The equilibrium solution is a simple caulinoïd [Eq. (9)] parameterized by θ_0 . Dashed lines show the horizontal and upside-down solutions. (c) Shape adopted by a wheat coleoptile (reproduced from [9], courtesy of B. Mouliia) with overlaid caulinoïd.

When $\omega \rightarrow \infty$, the plant remains straight with $\Lambda = \Theta = 0$ [Fig. 4(c)]. The equilibrium curve is uniquely determined by Λ and Θ . Experimentally, given ω , both parameters α and β can thus be estimated uniquely from the centerline (unlike in the planar case), e.g., by using the height of the plant $H = \tilde{z}(1) = \log(\cosh \Theta)/\Theta$ and the radius of the caulinoïd at the base $R = 1/\Lambda$.

A numerical linear stability analysis of the full system conducted across a wide range of realistic parameters $\lambda \in [0.1, 100]$ [Fig. 3(c)], consistent with reported values [9,13,32], reveals that, for $\beta > 0$, the equilibrium solution is linearly stable (Appendix D). Further, the local dynamics near the base can be obtained asymptotically, showing that the Darboux vector spirals towards its equilibrium value with a typical exponential decay $e^{-\beta t}$ [see Fig. 4(d) and Movie 1 in the Supplemental Material [33]]. In the limit case $\beta = 0$ but with $\omega \neq 0$ [1], the equilibrium solution is a segment of a horizontal circle of radius ω/α . Here, however, the previous stability result does not apply and the shoot “orbits” around

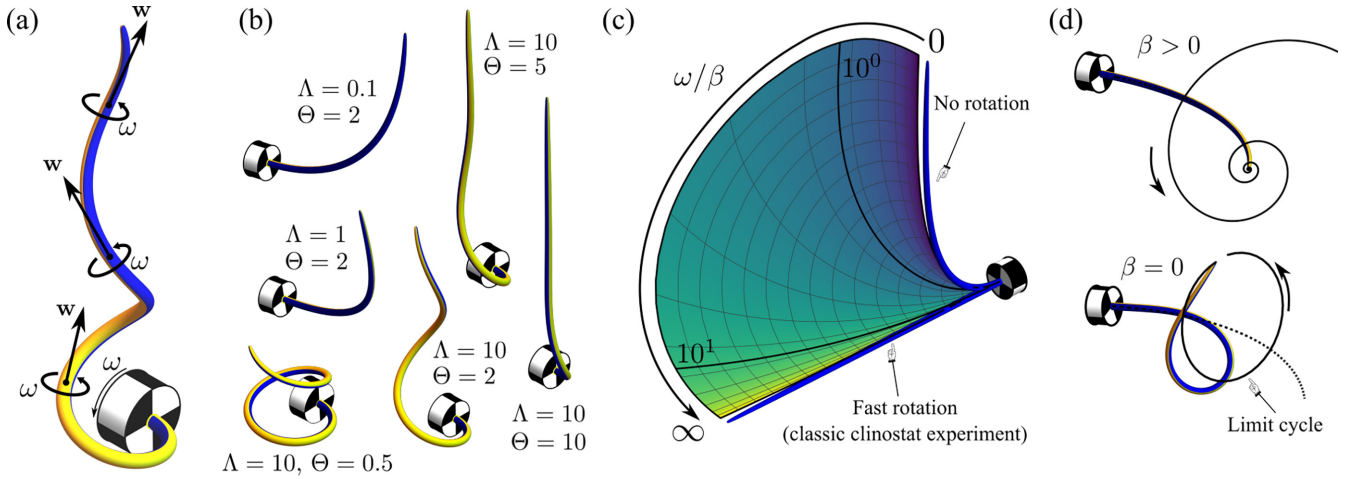


FIG. 4. Dynamic equilibrium of a clinostatting plant. (a) The material revolves at angular speed ω around a fixed centerline. (b) Example equilibrium configurations obtained for various values of Λ and Θ . (c) Dependency of the equilibrium solution on ω . Blue rods show the limits $\omega \rightarrow 0$ (no rotation) and $\omega \rightarrow \infty$ (standard clinostat experiment). The surface shows the set of equilibrium solutions obtained for finite values of ω/β ($\lambda = 5$). (d) Dynamic solution. Course of the apex in two cases, $\beta > 0$, with convergence to equilibrium ($\beta = \omega/5$), and $\beta = 0$, after convergence to a limit cycle (in both cases $\alpha = \omega$). Dashed line shows the corresponding equilibrium solution.

the equilibrium; see Fig. 4(d) and Movie 2 [33], showing numerically simulated solutions (Appendix C).

IV. SHOOT ELONGATION

Plants also lengthen due to the coordinated expansion of the cells along the central axis. Generally this primary growth is mostly confined to a region close to the apex [34]. To model elongation, including apical dominance, we assume that both the tropic response and axial growth gradually diminish as we move away from the apex with exponential decay of characteristic length δ and with growth Γ_0 and autogravitropic rates, β and α , at the tip (Appendix E). In this case, the system supports a traveling front solution connecting a flat base to a steady apical structure migrating forward at a speed $c = \Gamma_0\delta$ [see Fig. 5(a) and Movie 3 [33]]. The shape of this solitary wave can be described in terms of an initial value problem that can be integrated numerically. Figure 5(b) shows example solutions obtained for various rotation speeds and bending numbers λ . An interesting limit is $\ell \ll \delta$ (uniform growth rates along the shoot). Assuming a timescale separation $\beta \gg \Gamma_0$, and noting that Λ and Θ are independent of ℓ , we see that the shoot's shape will progress quasistatically, spreading itself uniformly along a unique caulinoïd [see Fig. 5(d) and Movie 4 [33]]. Overall, the existence of these solutions demonstrates that steady configurations are a robust property of the system that can persist even upon significant elongation.

V. DISCUSSION

The clinostat holds a significant place in plant physics, addressing a precise technical challenge: simulating weightlessness by effectively “confusing” the plant through fast rotation. At lower speeds, the interaction between rotation, gravitropism, and autotropism reveals more subtle behaviors. A distinct property of this system is the universal existence of a *dynamic* equilibrium where the shoot revolves around a steady centerline, the caulinoïd. This equilibrium is dy-

namic as it requires cyclic deformations in the material to maintain this configuration as rotation is applied. In contrast to the classic planar case, whose equilibrium is determined solely by λ (Fig. 3), this solution is *uniquely* characterized through two dimensionless numbers $\alpha\ell/\omega$ and β/ω . When the plant undergoes elongation, two distinct behaviors emerge: solitary waves when growth, autotropism, and gravitropism are confined to the tip, or stationary elongation along a unique caulinoïd when the shoot grows uniformly. In conclusion, we predict that a clinostatting shoot will naturally assume the sole shape that enables it to counterbalance rotation and minimize

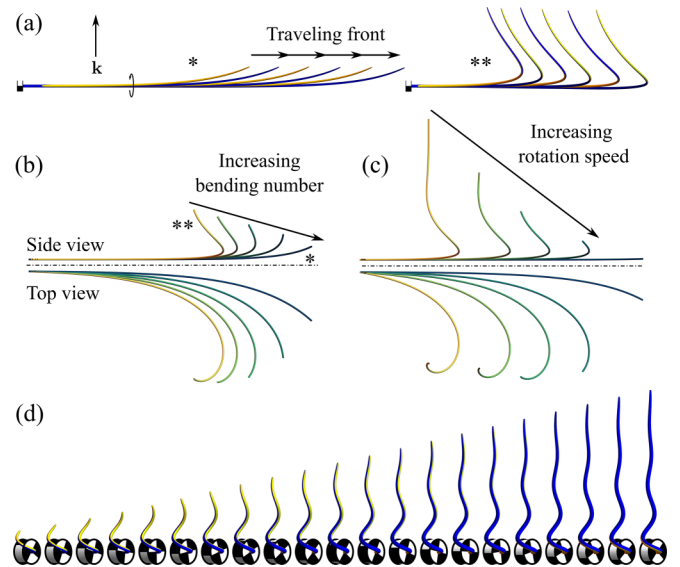


FIG. 5. Shoot elongation: (a) examples of simulated growing shoots (parameters: $\alpha = \omega$ and 5ω ; $\beta = \omega$; $\delta = \ell$; $\Gamma_0 = \omega/10$). (b, c) Solitary wave profiles computed for different (b) bending numbers λ and (c) rotation speeds ω . The labels * and ** indicate corresponding sets of parameters between the simulation and the asymptotic profile. (d) Uniform growth rate ($\delta \gg \ell$). The plant spreads along a unique caulinoïd ($\Lambda = 5$, $\Theta = 1$, $\Gamma_0 = \omega/10$).

its overall movement in the laboratory frame, strikingly, even in the absence of a dedicated rotation-sensing mechanism.

The importance of proprioception in plant posture control is now well established [2,3,9,15,35,36]. We further showed that the role of proprioception, in the form of autotropism, is crucial in stabilizing the clinostatting shoot, as its absence would lead to nonsteady behaviors [1]. These nonsteady behaviors of the sine law can be now understood as a direct consequence of the conservative nature of the sine-Gordon equation. Physically, autotropism acts as a damping (i.e., energy-dissipating) mechanism in curvature space, hence providing a stabilization mechanism for the universal shapes that we have uncovered. The exact caulinoïd solutions may be difficult to observe experimentally with precision as it would require pristine conditions. In plants, heterogeneity, stochasticity, memory effects [37,38], and other tropic responses also play a role. Yet these ideal solutions present a new paradigm for the study of plant active properties and the design of experiments. They can be further generalized to include other effects, such as light or elasticity [1]. Crucially, the slow clinostat, through its consistent disruption of the plant's equilibrium, allows for the establishment of adaptable and prolonged conditions for observing the out-of-equilibrium responses of the system, encompassing phenomena such as biological fatigue (generally any process that may affect the response capability of the system on a long timescale), or temporal integration effects such as frequency filtering.

Finally, the static and dynamic equilibria demonstrate that the coupling of internal and external regulation mechanisms is key for shape control, a problem of general importance in biology and active matter physics [39] with direct implications for nonliving active materials [40,41]. While these ideas have surfaced in different contexts previously, plants have predominantly been explored under specific conditions: (i) the planar case, (ii) the linear case, and (iii) in a static environment. In contrast, our contribution offers a comprehensive perspective, presenting a full, nonlinear, dynamic, three-dimensional treatment of the problem.

Our analysis of the clinostat problem provides a paradigm for deciphering experimentally the mechanisms through which an organism develops robustly under changing environmental conditions, and for studying dynamic, out-of-equilibrium aspects of living matter.

All numerical methods were implemented in *Wolfram Mathematica 13.0*. Source code is available upon request.

ACKNOWLEDGMENTS

A.G. acknowledges support from the Engineering and Physical Sciences Research Council of Great Britain under Research Grant No. EP/R020205/1. H.A.H. acknowledges support from the Royal Society under University Research Fellowship No. URF/R/211032, and from the Engineering and Physical Sciences Research Council of Great Britain under Research Grants No. EP/R018472/1 and No. EP/R005125/1. H.A.H. and H.O. acknowledge Research support from St John's College, Oxford.

APPENDIX A: KINETICS OF CURVATURE EVOLUTION

We summarize here the derivation of the kinetic model for curvature evolution, Eq. (6).

1. Local coordinates

We introduce Antman's sans-serif notation [42] to denote a vector field attached to a curve and expressed in the local material frame \mathbf{d}_i . Namely, for a vector field $\mathbf{u}(s, t)$, we write

$$\mathbf{u}(s, t) = \sum_{i=1}^3 u_i(s, t) \mathbf{d}_i(s, t), \quad (\text{A1})$$

where $u_i = \mathbf{u} \cdot \mathbf{d}_i$ denotes the i th local coordinate, with $i = 1, 2, 3$. Similarly, we note $\mathbf{u} = (u_1, u_2, u_3)$, the vector of local coordinates. Differentiating Eq. (A1) with respect to time, and using $\dot{\mathbf{d}}_i = \mathbf{w} \times \mathbf{d}_i$ [Eq. (3)], we obtain the kinematic relation

$$\dot{\mathbf{u}} + \mathbf{u} \times \mathbf{w} = \sum_{i=1}^3 \dot{u}_i \mathbf{d}_i, \quad (\text{A2})$$

which will be useful in the next section.

2. Kinetics

The kinetics of curvature evolution [Eq. (6)] is derived in [1]. The model is based on the Cholodny-Went paradigm of auxin-driven curvature evolution, which states that curvature emerges from a heterogeneous distribution of the growth hormone auxin at the scale of a cross section [43]. A summary of the model's assumptions and developments is given here; we refer to [1] for more details.

The starting point of the model is to define a scalar field $A(\mathbf{x}_1, \mathbf{x}_2, s)$ which models the concentration of auxin at a given point $\mathbf{p} = x_1 \mathbf{d}_1(s) + x_2 \mathbf{d}_2(s)$ in the cross section Ω_s located at the arclength s of the centerline. We assume that a tilt with respect to the vertical induces a flux of auxin, taken to be of the form $\mathbf{j} := -vA(\mathbf{k}_1 \mathbf{d}_1 + \mathbf{k}_2 \mathbf{d}_2)$, with $v > 0$ is a constant transport velocity, and with $\mathbf{k}_i = \mathbf{k} \cdot \mathbf{d}_i$ for $i = 1, 2, 3$, where \mathbf{k} is the vertically aligned unit vector (i.e., the opposite direction of gravity). This constitutive assumption models an active flow of auxin towards the downward side of the cross section and may be viewed as a simplification of the starch-statolith hypothesis [26,27] and the so-called position sensor hypothesis [44,45]. The flux \mathbf{j} of auxin is included in a continuity equation expressing conservation of auxin mass, taking the general form

$$\frac{\partial A}{\partial t} + \nabla \cdot \mathbf{j} = S - k_{\text{off}} A, \quad (\text{A3})$$

where $\nabla := \partial/\partial x_1 \mathbf{d}_1 + \partial/\partial x_2 \mathbf{d}_2 + \partial/\partial s \mathbf{d}_3$ is the standard Del operator, k_{off} denotes an absorption/decay rate of auxin, and S symbolizes any source or sink whose specific expression is detailed in [1]. Next, we focus on the steady regime of Eq. (A3), given by

$$v \nabla \cdot (A(\mathbf{k}_1 \mathbf{d}_1 + \mathbf{k}_2 \mathbf{d}_2)) + k_{\text{off}} A = S. \quad (\text{A4})$$

To model auxin-mediated growth, a second constitutive equation is then introduced that couples the rate $\dot{g}(\mathbf{x}_1, \mathbf{x}_2, s)$ of cell *axial* expansion, i.e., expansion along \mathbf{d}_3 , to the

concentration of auxin A . A simple growth law, capturing auxin-mediated growth and autotropism, is

$$\dot{g} = c_1(A - A^*) - c_2(g - \bar{g}). \quad (\text{A5})$$

The first term on the right-hand side states that the growth rate increases (if $c_1 > 0$) with the level of auxin above a baseline level A^* . Generally, the rate constant c_1 will be taken to be positive in shoots doing *negative gravitropism*, where the growth rate increases with the presence of auxin. Conversely, c_1 will be typically taken to be negative in roots that exhibit *positive gravitropism* and where higher levels of auxin correlate with slower growth. The second term on the right-hand side mimics the effect of autotropism (with rate constant $c_2 \geq 0$) by penalizing deviations of the growth field from its average level

$$\bar{g} := \frac{1}{\mathcal{A}} \int_{\Omega_s} g(\mathbf{x}_1, \mathbf{x}_2, s) d\mathbf{x}_1 d\mathbf{x}_2 \quad (\text{A6})$$

(\mathcal{A} is the cross-sectional area, taken to be constant).

Lastly, the goal is to perform a dimensional reduction of the model, from three dimensions (tissue continuum) to one dimension (curve) to derive a *rod theory*. On averaging the growth field over the cross section, following the dimensional-reduction procedure detailed in [30], we obtain

$$\mathcal{I}_1 u_1(s, t) = \int_{\Omega_s} \mathbf{x}_2 g(\mathbf{x}_1, \mathbf{x}_2, s) d\mathbf{x}_1 d\mathbf{x}_2, \quad (\text{A7a})$$

$$\mathcal{I}_2 u_2(s, t) = - \int_{\Omega_s} \mathbf{x}_1 g(\mathbf{x}_1, \mathbf{x}_2, s) d\mathbf{x}_1 d\mathbf{x}_2, \quad (\text{A7b})$$

where \mathcal{I}_1 and \mathcal{I}_2 denote the second moments of area around \mathbf{d}_1 and \mathbf{d}_2 respectively. Here we assume a symmetric and centered cross section such that $\mathcal{I}_1 = \mathcal{I}_2$, and

$$\int_{\Omega_s} \mathbf{x}_1 d\mathbf{x}_1 d\mathbf{x}_2 = \int_{\Omega_s} \mathbf{x}_2 d\mathbf{x}_1 d\mathbf{x}_2 = 0. \quad (\text{A8})$$

Since the cross section does not vary with time, the curvatures evolve according to

$$\mathcal{I}_1 \dot{u}_1(s, t) = \int_{\Omega_s} \mathbf{x}_2 \dot{g}(\mathbf{x}_1, \mathbf{x}_2, s) d\mathbf{x}_1 d\mathbf{x}_2, \quad (\text{A9a})$$

$$\mathcal{I}_2 \dot{u}_2(s, t) = - \int_{\Omega_s} \mathbf{x}_1 \dot{g}(\mathbf{x}_1, \mathbf{x}_2, s) d\mathbf{x}_1 d\mathbf{x}_2. \quad (\text{A9b})$$

The dimensional reduction also yields

$$u_3 = 0 \quad (\text{A10})$$

meaning that the rod is twistless. Inserting Eq. (A5) into Eq. (A9) and using Eq. (A8) to eliminate the terms with A^* and \bar{g} gives an equation for \dot{u}_1 in terms of u_1 itself and the integral of $\mathbf{x}_2 A$, and similarly for u_2 . The integral can be computed by replacing A via Eq. (A4) and repeated applications of the divergence theorem along with a no-flux condition on the cross-sectional boundary (for full details see the Supplementary Material of [1]). This manipulation yields the local autogravitropic laws given by

$$\dot{u}_1 = -\alpha k_2 - \beta u_1, \quad (\text{A11a})$$

$$\dot{u}_2 = \alpha k_1 - \beta u_2, \quad (\text{A11b})$$

where α and β are lumped parameters that emerge from the homogenization. Since $\dot{u}_3 = -\beta u_3$ is trivially satisfied in

virtue of Eqs. (A10), Eqs. (A11) can be written in a more compact vector form as

$$\dot{\mathbf{u}} = \alpha \mathbf{t} \times \mathbf{k} - \beta \mathbf{u}. \quad (\text{A12})$$

Equation (A12) expresses the evolution of curvatures from a local point of view, i.e., in a reference frame attached to the material. In our case, since global gravity is important, it is convenient to express the dynamics in the nonrotating, laboratory frame. Indeed, the equilibrium solutions are naturally expressed in the laboratory frame, whereas in the local frame, the dynamic equilibrium is associated with T -periodic variables. As can be seen, Eq. (A12) is equivalent to Eq. (6). Indeed, using the kinematic formula (A2) and the rotational invariance of the cross product, Eq. (A12) can be rewritten in the laboratory frame as in Eq. (6).

APPENDIX B: EQUILIBRIUM SOLUTIONS

1. Without rotation

We derive the equilibrium solutions for the nonrotating case ($\omega = 0$). Here we choose $\ell \equiv 1$ as a reference length unit. Setting $\dot{\mathbf{u}} = \mathbf{0}$ and $\mathbf{w} = \mathbf{0}$ in Eq. (6) provides $\tilde{\mathbf{u}} = \lambda \tilde{\mathbf{t}} \times \mathbf{k}$, which can be substituted into Eq. (5) to obtain

$$\tilde{\mathbf{t}}' = \lambda (\tilde{\mathbf{t}} \times \mathbf{k}) \times \tilde{\mathbf{t}}. \quad (\text{B1})$$

Provided an initial tilt $0 \leq \theta_0 < \pi$, such that $\tilde{\mathbf{t}}(0) = \sin \theta_0 \mathbf{i} + \cos \theta_0 \mathbf{k}$, we integrate this equation and derive the tangent

$$\tilde{\mathbf{t}}(s) = \frac{\sin \theta_0}{\cos \theta_0 \sinh \lambda s + \cosh \lambda s} \mathbf{i} + \frac{(\cos \theta_0 + 1)e^{2\lambda s} - 1 + \cos \theta_0}{(\cos \theta_0 + 1)e^{2\lambda s} + 1 - \cos \theta_0} \mathbf{k}. \quad (\text{B2})$$

Integrating once more gives the position vector $\tilde{\mathbf{r}}(s) = \tilde{x}(s) \mathbf{i} + \tilde{z}(s) \mathbf{k}$:

$$\lambda \tilde{x}(s) = \theta_0 - 2 \operatorname{arccot} \left(e^{\lambda s} \cot \frac{\theta_0}{2} \right), \quad (\text{B3a})$$

$$\lambda \tilde{z}(s) = \log[1 + \cos^2(\theta_0/2)(e^{2\lambda s} - 1)] - \lambda s. \quad (\text{B3b})$$

Inverting Eq. (B3a) and rescaling all lengths as $\tilde{x} \rightarrow \tilde{x}/\lambda$, $\tilde{z} \rightarrow \tilde{z}/\lambda$, we obtain an implicit relation between \tilde{z} and \tilde{x} [Eq. (9)], which corresponds to a universal equilibrium shape for all orientations θ_0 of the shoot.

2. With rotation

Next, we derive the equilibrium solution for a plant undergoing rotation ($\omega > 0$). To determine the equilibrium shape, we posit $\dot{\mathbf{w}} = \dot{\mathbf{t}} = \dot{\mathbf{u}} = \mathbf{0}$. Equations (3) and (4) directly provide that $\tilde{\mathbf{w}} = \omega \tilde{\mathbf{t}}$. Substituting this ansatz into Eq. (6), we obtain

$$\beta \tilde{\mathbf{u}} = \tilde{\mathbf{t}} \times (\alpha \mathbf{k} + \omega \tilde{\mathbf{u}}). \quad (\text{B4})$$

On inverting this identity, we can express $\tilde{\mathbf{u}}$ as an explicit function of $\tilde{\mathbf{t}}$, given by

$$\tilde{\mathbf{u}} = (\Lambda \tilde{t}_1 \tilde{t}_3 + \Theta \tilde{t}_2) \mathbf{i} + (\Lambda \tilde{t}_2 \tilde{t}_3 - \Theta \tilde{t}_1) \mathbf{j} + \Lambda (\tilde{t}_3^2 - 1) \mathbf{k}, \quad (\text{B5})$$

with $\tilde{\mathbf{t}} = \tilde{t}_1 \mathbf{i} + \tilde{t}_2 \mathbf{j} + \tilde{t}_3 \mathbf{k}$. Substituting this last expression into Eq. (5) and integrating it, we obtain the expression for the

tangent given by Eq. (10). Remarkably, we can integrate the tangent to obtain an exact parametrization of the centerline

$$\tilde{x}(s) = \frac{e^{s(\Theta+i\Lambda)}}{\Theta+i\Lambda} {}_2F_1\left(1, \frac{\Theta+i\Lambda}{2\Theta}; \frac{3\Theta+i\Lambda}{2\Theta}; -e^{2s\Theta}\right) + \frac{e^{s(\Theta-i\Lambda)}}{\Theta-i\Lambda} {}_2F_1\left(1, \frac{\Theta-i\Lambda}{2\Theta}; \frac{3\Theta-i\Lambda}{2\Theta}; -e^{2s\Theta}\right) - \frac{\pi}{2\Theta} \operatorname{sech}\left(\frac{\pi\Lambda}{2\Theta}\right), \quad (\text{B6a})$$

$$\tilde{y}(s) = \frac{i}{4\Theta} \left[\psi^{(0)}\left(\frac{\Theta+i\Lambda}{4\Theta}\right) - \psi^{(0)}\left(\frac{3\Theta+i\Lambda}{4\Theta}\right) + H_{-\frac{\Theta+i\Lambda}{4\Theta}} - H_{-\frac{3\Theta+i\Lambda}{4\Theta}} \right] + \frac{e^{s(\Theta+i\Lambda)}}{\Lambda-i\Theta} {}_2F_1\left(1, \frac{\Theta+i\Lambda}{2\Theta}; \frac{3\Theta+i\Lambda}{2\Theta}; -e^{2s\Theta}\right) + \frac{e^{s(\Theta-i\Lambda)}}{\Lambda+i\Theta} {}_2F_1\left(1, \frac{\Theta-i\Lambda}{2\Theta}; \frac{3\Theta-i\Lambda}{2\Theta}; -e^{2s\Theta}\right), \quad (\text{B6b})$$

$$\tilde{z}(s) = \frac{\log[\cosh(\Theta s)]}{\Theta}. \quad (\text{B6c})$$

Figure 6 shows the set of solution shapes for different values of Λ and Θ . Inset shows the path of the solution in the κ - τ space, which follows the ellipse given by Eq. (11).

APPENDIX C: NUMERICAL RESOLUTION OF THE NONLINEAR SYSTEM

We use a method based on Chebyshev polynomials to integrate numerically the nonlinear system given by Eqs. (4)–(7). We first remark that the system, albeit originally

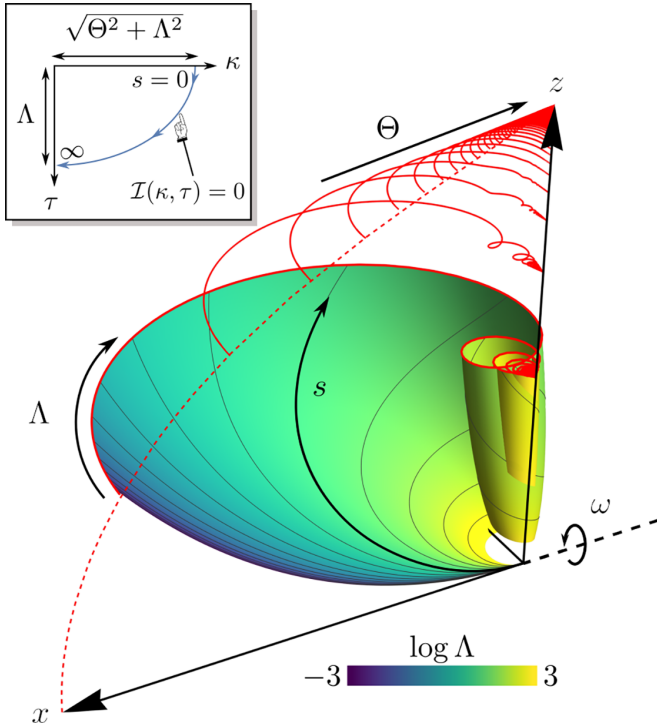


FIG. 6. Set of equilibrium solutions. The colored surface plot sweeps solutions for a range of Λ (with $\Theta = 1$). Red solid lines show the course of the shoot tip $s = 0$ as Λ varies, and for different values of $\Theta > 1$, with height given by $h(\Theta) = \log(\cosh \Theta)/\Theta$. Red dashed line shows the tip position for $\Lambda = 0$ as a function of Θ , given by $(x(\Theta), z(\Theta)) = (g\Theta/\Theta, h(\Theta))$. Inset shows the path of the solution in the κ - τ plane [Eq. (11)].

$\tilde{\mathbf{r}}$, in terms of the hypergeometric function ${}_2F_1$, the harmonic number H_n and the polygamma function of order zero $\psi^{(0)}$:

defined for $s \in [0, 1]$, can be extended naturally to $s \in [-1, 1]$ (by considering two “twin” shoots oriented opposite to each other with respect to the plane y - z). Here the extended equilibrium solution is invariant with respect to the mirror symmetry $x \rightarrow -x$, $s \rightarrow -s$. This situation is ideal for using Chebyshev polynomials (of the first kind) T_n [46] as they are defined canonically on $[-1, 1]$. Thus, we consider the truncated Chebyshev expansions for the variables

$$\mathbf{t} \approx \sum_{n=0}^N \mathbf{T}^n T_n, \quad (\text{C1a})$$

$$\mathbf{w} \approx \sum_{n=0}^N \mathbf{W}^n T_n, \quad (\text{C1b})$$

$$\mathbf{u} \approx \sum_{n=0}^N \mathbf{U}^n T_n, \quad (\text{C1c})$$

with N a positive integer.

The formal solutions for \mathbf{t} and \mathbf{w} ,

$$\mathbf{t} = \mathbf{i} + \int_0^s \mathbf{u} \times \mathbf{t}, \quad (\text{C2a})$$

$$\mathbf{w} = \omega \mathbf{i} + \alpha \int_0^s \mathbf{t} \times \mathbf{k} - \beta \int_0^s \mathbf{u}, \quad (\text{C2b})$$

can be decomposed in the Chebyshev basis as follows. From the products $T_n T_m = (T_{n+m} + T_{|n-m|})/2$ [46], we derive the expansion of the cross products; i.e., for any vector field \mathbf{a} and \mathbf{b} with respective Chebyshev coefficients \mathbf{A}^n and \mathbf{B}^n , we have

$$\mathbf{a} \times \mathbf{b} = \frac{1}{2} \sum_{p=0}^{\infty} (\mathbf{A}^p \times \mathbf{B}^p + \mathbf{A}^p \times \mathbf{B}^{-p}) T_0 + \frac{1}{2} \sum_{n=1}^{\infty} \sum_{p=0}^n (\mathbf{A}^p \times \mathbf{B}^{n-p} + \mathbf{A}^p \times \mathbf{B}^{n+p} + \mathbf{A}^{n+p} \times \mathbf{B}^p) T_n. \quad (\text{C3})$$

For integration, we use the recurrence formulas [46]

$$\int T_0 = T_1, \quad \int T_1 = \frac{1}{4}(T_2 + T_0), \quad (\text{C4a})$$

$$\int T_n = \frac{1}{2} \left(\frac{T_{n+1}}{n+1} - \frac{T_{n-1}}{n-1} \right), \quad \forall n \geq 2, \quad (\text{C4b})$$

to obtain

$$\int \mathbf{a} = \frac{\mathbf{A}^1}{4} T_0 + \mathbf{A}^0 T_1 + \sum_{n=2}^{\infty} \frac{\mathbf{A}^{n-1} - \mathbf{A}^{n+1}}{2n} T_n. \quad (\text{C5})$$

Conveniently, integration corresponds to a linear operation on the \mathbf{A}^n , whose matrix can be precomputed.

Given the coefficients \mathbf{U}^n , the Chebyshev expansion of Eq. (C2a) yields a linear system that can be inverted to obtain the \mathbf{T}^n . Then the \mathbf{W}^n are obtained by direct integration, using Eq. (C5). After expressing the \mathbf{T}^n and \mathbf{W}^n as functions of the \mathbf{U}^n , we obtain a dynamical system of the form

$$\dot{\mathbb{U}}^N = \mathcal{F}(\mathbb{U}^N), \quad (\text{C6})$$

where \mathbb{U}^N is the $3(N+1)$ -dimensional vector formed by the concatenation of the \mathbf{U}^n ; and \mathcal{F} is a second-degree polynomial vector that is evaluated numerically. Provided appropriate initial conditions, Eq. (C6) can be integrated numerically using a standard IVP solver (here we used *Mathematica*'s built-in routine *NDSolve*).

A general problem is to find an initial condition for \mathbf{u} that satisfies the orthogonality condition, Eq. (7). Indeed, by differentiating $\mathbf{u} \cdot \mathbf{t}$ with respect to time and using Eq. (6), we observe that

$$\frac{\partial}{\partial t} (\mathbf{u} \cdot \mathbf{t}) = -\beta \mathbf{u} \cdot \mathbf{t}. \quad (\text{C7})$$

Since $\beta > 0$, Eq. (7) is a stable property, in particular, if Eq. (7) is satisfied at $t = 0$, it will be automatically satisfied at all times t . Note that, if $\mathbf{u} \cdot \mathbf{t} = 0$, then we have automatically

$$\mathbf{u} = \mathbf{t} \times \mathbf{t}' \quad (\text{C8})$$

(the converse is trivial). Thus a suitable initial condition can always be found by first defining a curve and its tangent \mathbf{t} , and then obtaining \mathbf{u} through Eq. (C8). Once an initial configuration is defined, the initial Chebyshev coefficients for $\mathbb{U}^N(0)$ are computed efficiently by means of the discrete cosine transform [47].

1. Convergence analysis

We here provide a comment on the influence of N on the accuracy of the solver. Given a resolution N we can embed a solution \mathbb{U}^N vector in an infinite-dimensional real space by adopting the convention

$$\mathbb{U}_n^N = 0 \quad (\text{C9})$$

for all $n > 3(N+1)$. The exact steady solution $\tilde{\mathbf{u}}$ is known, and its Chebyshev coefficients can be computed. The distance of the solution at a given time t , to the actual fixed point is defined as

$$\mathcal{D}_N(t) = \sqrt{\sum_{n=0}^{\infty} (\mathbb{U}_n^N(t) - \tilde{\mathbb{U}}_n)^2} \quad (\text{C10})$$

(the existence of the sum is ensured by Parseval's theorem). A measure of the convergence error for the solver is obtained by considering the limit of $\mathcal{D}_N(t)$ as $t \rightarrow \infty$. Indeed, for a perfectly accurate solver, we expect $\mathcal{D}_N(t) \rightarrow 0$ since the

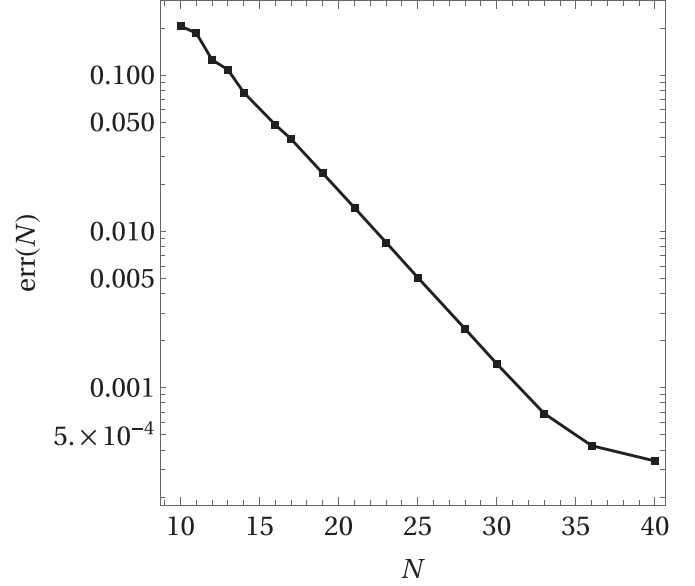


FIG. 7. Logarithmic plot of the asymptotic accuracy error $\text{err}(N)$ [Eq. (C11)] vs N .

equilibrium is unique and stable. We then define the asymptotic accuracy error as

$$\text{err}(N) = \frac{\lim_{t \rightarrow \infty} \mathcal{D}_N(t)}{\sqrt{\sum_{n=0}^{\infty} \tilde{\mathbb{U}}_n^2}}. \quad (\text{C11})$$

A plot of $\text{err}(N)$ obtained for various values of N and for realistic parameters ($\alpha = 10\omega$, $\beta = \omega$) is shown in Fig. 7, showing exponential convergence.

APPENDIX D: STABILITY

1. Asymptotic analysis near the base

To gain insight into the dynamics of the shoot and the stability of the equilibrium, it is useful to first restrict our attention to the base of the plant, $s = 0$, where $\mathbf{t}(0, t) = \mathbf{i}$ and $\mathbf{w}(0, t) = \omega \mathbf{i}$. Letting $\mathbf{U}(t) = \mathbf{u}(0, t)$, Eq. (6) reduces to

$$\dot{U}_2 = -\alpha - \beta U_2 - \omega U_3, \quad \dot{U}_3 = \omega U_2 - \beta U_3 \quad (\text{D1})$$

with $\mathbf{U} = U_1 \mathbf{i} + U_2 \mathbf{j} + U_3 \mathbf{k}$. We have $U_1 = 0$ by Eq. (7). The system admits a unique fixed point $(U_2, U_3) = (-\Theta, -\Lambda)$ (this is simply the equilibrium curvatures at the origin derived in Appendix B 2), associated with a pair of conjugate eigenvalues $-\beta \pm \omega i$ with a negative real part: The fixed point is a spiral sink associated with a decaying amplitude $\sim e^{-\beta t}$ and rotation speed ω . When $\beta = 0$ the fixed point is a center, and the solution orbits around the fixed point.

We can extend this analysis to higher orders in $s > 0$ in principle (that is, expanding all variables in orders of s and performing a regular perturbation analysis). For instance, Fig. 8 shows the second-order approximation of the solution taken at $s = 0.25$. The second-order estimate converges towards equilibrium when $\beta > 0$ and $s \ll 1$ (in the case $\beta = 0$, however, there is a secular term that must be treated by a dedicated method, but we leave this problem outside the scope of this study, focusing on the physiologically relevant case $\beta > 0$).

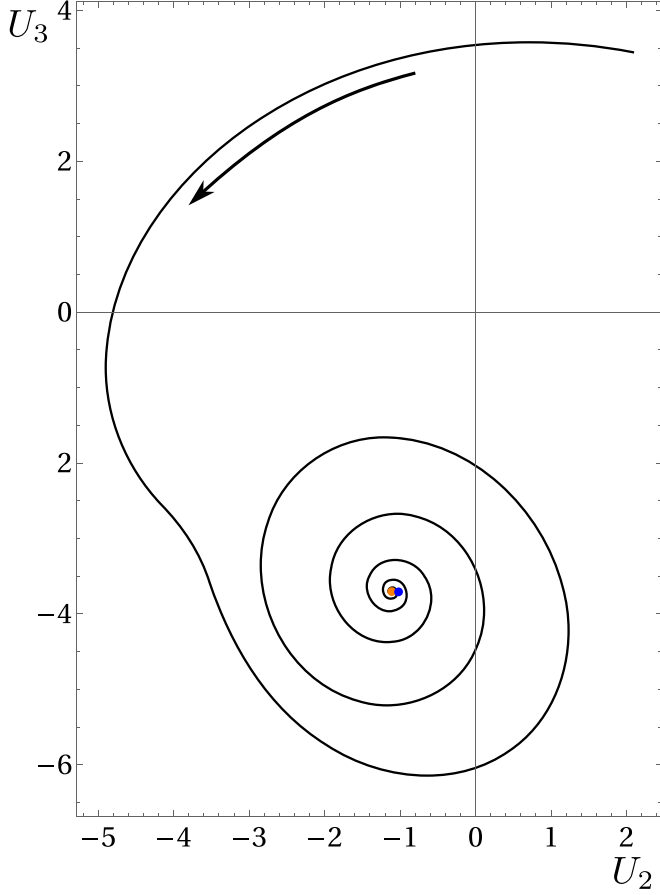


FIG. 8. Example course of the Darboux vector $\mathbf{U}(t)$ in the \mathbf{j} - \mathbf{k} plane, computed asymptotically (to second order in s) near the base ($s = 0.25$). The asymptotic solution spirals towards an equilibrium value ($\alpha = 4\omega$, $\beta = 0.2\omega$). Blue and orange dots show the exact value of \mathbf{u} at equilibrium at s and its second-order approximation, respectively.

2. Linear stability analysis

The previous analysis provides insight into the dynamics of the system; however, in principle, it is valid only near the base. To complement that approach, we perform a linear stability analysis of the equilibrium solution. Therefore, we take the first variation of Eqs. (4) to (7) around the base equilibrium solution derived in Appendix B 2. Rearranging the terms, we obtain

$$\delta \mathbf{t}' = \delta \mathbf{u} \times \tilde{\mathbf{t}} + \tilde{\mathbf{u}} \times \delta \mathbf{t}, \quad (\text{D2a})$$

$$\delta \mathbf{w}' = \alpha \delta \mathbf{t} \times \mathbf{k} - \beta \delta \mathbf{u}, \quad (\text{D2b})$$

$$\delta \dot{\mathbf{u}} = \delta \mathbf{w}' + \delta \mathbf{w} \times \tilde{\mathbf{u}} + \tilde{\mathbf{w}} \times \delta \mathbf{u}, \quad (\text{D2c})$$

with the conditions

$$\tilde{\mathbf{u}} \cdot \delta \mathbf{t} = -\delta \mathbf{u} \cdot \tilde{\mathbf{t}}, \quad \tilde{\mathbf{t}} \cdot \delta \mathbf{t} = 0. \quad (\text{D3})$$

The boundary conditions at $s = 0$ fix the values of $\mathbf{t}(0, t)$ and $\mathbf{w}(0, t)$, thus,

$$\delta \mathbf{t}(0, t) = \mathbf{0}, \quad \delta \mathbf{w}(0, t) = \mathbf{0}. \quad (\text{D4})$$

We start by solving Eq. (D2a). As can be seen, a linearly independent basis of solutions for the homogeneous part of

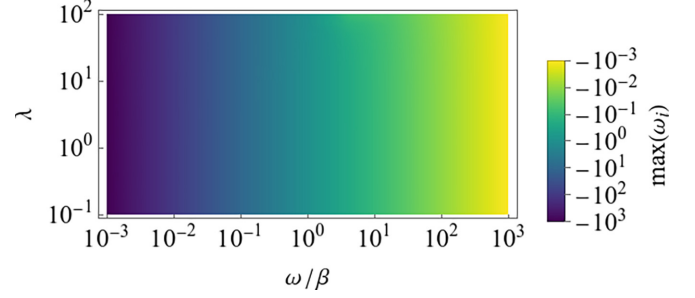


FIG. 9. Numerical linear stability analysis. Density plot showing the value of the largest real part ω_i of the eigenvalues of Eq. (D6) (to generate this plot, the system was re-expressed in terms of the dimensionless time ωt). This shows that the dynamics is dominated by a decay rate of order $e^{-\beta t}$ as expected from Appendix D 1.

Eq. (D2a) is provided by the \mathbf{d}_i at equilibrium (defined up to an arbitrary rotation of the clinostat). A particular solution is then obtained by means of variation of constants. For a given $\delta \mathbf{u}$, the solutions to Eqs. (D2a), (D2b), and (D4) are

$$\delta \mathbf{t} = \mathbf{d}_1 \int_0^s \delta \mathbf{u} \cdot \mathbf{d}_2 - \mathbf{d}_2 \int_0^s \delta \mathbf{u} \cdot \mathbf{d}_1, \quad (\text{D5a})$$

$$\delta \mathbf{w} = -\alpha \mathbf{k} \times \int_0^s \delta \mathbf{t} - \beta \int_0^s \delta \mathbf{u}. \quad (\text{D5b})$$

Last, we perform a Chebyshev spectral analysis of the linearized system. Namely, expanding Eqs. (D2c) and (D5) as in Appendix C, we obtain a linear dynamical system

$$\delta \dot{\mathbf{U}} = \mathbf{L} \delta \mathbf{U} \quad (\text{D6})$$

for the Chebyshev coefficients $\delta \mathbf{U}$. Note that, since the orthogonality constraint, Eq. (D3), is stable by Eq. (C7), we need not consider it in the stability analysis, as coordinates orthogonal to the constraint surface will vanish. The complex eigenvalues of \mathbf{L} can be computed numerically as illustrated in Fig. 9; specifically, the system is linearly stable if all the real parts $\omega_i \in \mathbb{R}^{3(N+1)}$ of these eigenvalues are negative. Here the system appears to be stable for all values of λ and ω tested. The results are consistent with the dynamics predicted in Appendix D 1, which is dominated by a decay rate of order $e^{-\beta t}$.

APPENDIX E: SHOOT ELONGATION

1. General model

To model growth, we introduce the standard growth multiplier $\gamma := \partial s / \partial s_0$ which connects the arclength $s_0 \in [0, \ell_0]$ in the initial configuration of the shoot, to the arclength $s \in [0, \ell(t)]$ in the current, grown configuration [21]. To account for apical dominance, we assume that growth and curvature generation mostly happen within a finite distal section of the stem of length δ . Therefore, we introduce an activation function:

$$a(s_0, t) = f(\ell(t) - s(s_0, t)), \quad (\text{E1})$$

with $f(\sigma) = e^{-\sigma/\delta}$, modeling the slowing down of growths as we move away from the tip of the shoot, located at

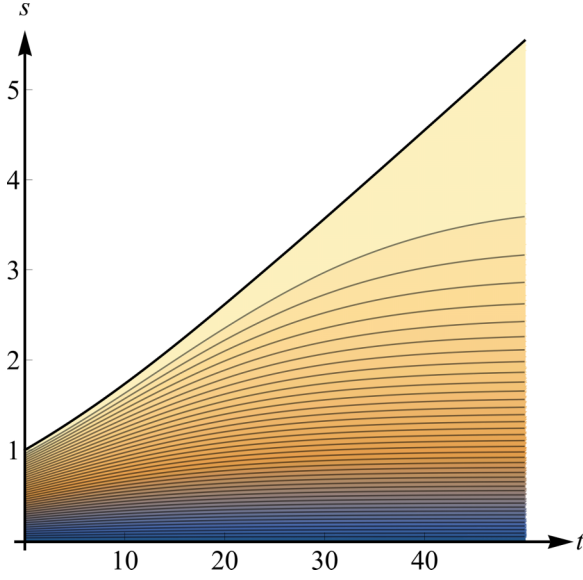


FIG. 10. Kymograph showing the apical growth field. Lines show the trajectories of the material points with initial arclength emphasized by colors.

$\ell(t) = s(\ell_0, t)$. A kymograph illustrating this growth profile is shown in Fig. 10. Accordingly, we assume an exponential growth kinetics given by [21]

$$\Gamma := \frac{\dot{\gamma}}{\gamma} = \Gamma_0 a(s_0, t), \quad (\text{E2})$$

which captures a type of growth where all cells in a small portion of the tissue expand and proliferate at the same rate. Similarly, we define the rates of curvature generation $A(s_0, t) = \alpha a(s_0, t)$ and $B(s_0, t) = \beta a(s_0, t)$. Note that the model can be easily adapted to include richer apical growth models, e.g., sigmoids [48]; however, we do not expect any significant qualitative change in the results.

On integrating the standard kinematic relation $\partial s / \partial t = \Gamma$ using Eqs. (E1) and (E2), we obtain

$$\dot{s} = c e^{-\ell/\delta} (e^{s/\delta} - 1), \quad (\text{E3})$$

with $c := \Gamma_0 \delta$ a characteristic speed; and where ℓ is governed by

$$\dot{\ell} = c(1 - e^{-\ell/\delta}), \quad (\text{E4})$$

as a particular case of Eq. (E3). Provided the initial condition $\ell(0) = \ell_0 \equiv 1$, the previous equation integrates as

$$\ell(t) = \delta \log((e^{1/\delta} - 1) e^{\Gamma_0 t} + 1). \quad (\text{E5})$$

Integrating Eq. (E3) with Eq. (E5) then gives

$$\begin{aligned} s(s_0, t) &= \delta \log \left[\frac{1}{2} - \frac{1}{2} \tanh \left(\frac{\Gamma_0 t}{2} + \frac{1}{2\delta} + \arctan(1 - 2e^{s_0/\delta}) \right) \right. \\ &\quad \left. - \frac{1}{2} \log((e^{1/\delta} - 1) e^{\Gamma_0 t} + 1) \right]. \end{aligned} \quad (\text{E6})$$

Thus,

$$a(s_0, t) = \left[\exp \left(\frac{ct + 1 - s_0}{\delta} \right) - e^{ct/\delta} + 1 \right]^{-1} \quad (\text{E7})$$

and

$$\gamma(s_0, t) = \left[(1 - e^{ct/\delta}) \exp \left(\frac{s_0 - ct - 1}{\delta} \right) + 1 \right]^{-1}. \quad (\text{E8})$$

In the context of a growing spatial domain, one must differentiate between the material (*Lagrangian*) derivative, denoted with an overdot $\dot{\mathbf{u}}$, and the *Eulerian* derivative denoted $\partial \mathbf{u} / \partial t$, and such that

$$\dot{\mathbf{u}} = \frac{\partial \mathbf{u}}{\partial t} + \dot{s} \frac{\partial \mathbf{u}}{\partial s}. \quad (\text{E9})$$

The vectors \mathbf{u} and \mathbf{w} are defined here in the Eulerian sense, namely, such that

$$\frac{\partial \mathbf{t}}{\partial s} = \mathbf{u} \times \mathbf{t}, \quad \frac{\partial \mathbf{t}}{\partial t} = \mathbf{w} \times \mathbf{t}, \quad (\text{E10})$$

with the compatibility condition

$$\frac{\partial \mathbf{u}}{\partial t} - \frac{\partial \mathbf{w}}{\partial s} = \mathbf{w} \times \mathbf{u}. \quad (\text{E11})$$

In contrast, the Lagrangian spin vector, $\mathbf{p} = \mathbf{w} + \dot{s} \mathbf{u}$, is associated with

$$\dot{\mathbf{i}} = \mathbf{p} \times \mathbf{t}. \quad (\text{E12})$$

The revised governing equations, including growth, are then

$$\mathbf{t}' = \gamma \mathbf{u} \times \mathbf{t}, \quad (\text{E13a})$$

$$\mathbf{p}' = \gamma (A \mathbf{t} \times \mathbf{k} - B \mathbf{u}), \quad (\text{E13b})$$

$$\dot{\mathbf{u}} + \mathbf{u} \times \mathbf{p} + \Gamma \mathbf{u} = \mathbf{p}' / \gamma, \quad (\text{E13c})$$

where $(\cdot)'$ denotes a derivative with respect to the Lagrangian coordinate s_0 . The extra term $\Gamma \mathbf{u}$ accounts for the passive decrease of curvature due to axial stretch. The presence of the factor γ simply results from the chain rule, as we have expressed the system with respect to s_0 .

2. Solitary waves

To derive the shape of self-similar, traveling-front solutions we introduce the comoving coordinate $\sigma := \ell - s$, measuring the arclength from the apex, with the base located at $\sigma = \ell \rightarrow \infty$. Setting $\partial \mathbf{u} / \partial t = \mathbf{0}$, Eq. (E13) becomes upon this change of coordinate

$$\frac{\partial \mathbf{t}}{\partial \sigma} = \mathbf{t} \times \mathbf{u}, \quad (\text{E14a})$$

$$\frac{\partial \mathbf{p}}{\partial \sigma} = f(\sigma) (\alpha \mathbf{k} \times \mathbf{t} + \beta \mathbf{u}), \quad (\text{E14b})$$

$$c f(\sigma) \frac{\partial \mathbf{u}}{\partial \sigma} + \frac{\partial \mathbf{p}}{\partial \sigma} = \mathbf{p} \times \mathbf{u} - \Gamma \mathbf{u}, \quad (\text{E14c})$$

with the conditions $\lim_{\sigma \rightarrow \infty} \mathbf{t} = \mathbf{i}$, $\lim_{\sigma \rightarrow \infty} \mathbf{p} = \omega \mathbf{i}$ and $\lim_{\sigma \rightarrow \infty} \mathbf{u} = \mathbf{0}$. In practice, the system can be integrated for $\sigma \in [0, \Sigma]$ with $\Sigma \gg \delta$, and with boundary conditions expressed at Σ . There is, however, a removable singularity at $\sigma \rightarrow \infty$, as $f(\sigma)$ is transcendently small, which causes

numerical difficulties in Eq. (E14c). To alleviate this issue, we consider perturbed boundary conditions of the form $\mathbf{t}(\Sigma) = \mathbf{i} + \epsilon_t(\Sigma)$, $\mathbf{p}(\Sigma) = \omega\mathbf{i} + \epsilon_p(\Sigma)$, and $\mathbf{u}(\Sigma) = \epsilon_u(\Sigma)$, where ϵ_t , ϵ_p , and ϵ_u denote small perturbations from the boundary con-

ditions at $\sigma = \infty$. Expanding Eq. (E14) and keeping only the higher order nonzero terms allows us to solve for ϵ_t , ϵ_p , and ϵ_u , in order to express the perturbed boundary values [Fig. 5(b) is obtained with $\Sigma \approx 5\delta$].

-
- [1] D. E. Moulton, H. Oliveri, and A. Goriely, *Proc. Natl. Acad. Sci. USA* **117**, 32226 (2020).
- [2] B. Moulia, R. Bastien, H. Chauvet-Thiry, and N. Leblanc-Fournier, *J. Exp. Bot.* **70**, 3467 (2019).
- [3] O. Hamant and B. Moulia, *New Phytol.* **212**, 333 (2016).
- [4] B. Moulia and M. Fournier, *J. Exp. Bot.* **60**, 461 (2009).
- [5] A. Johnsson, *Q. Rev. Biophys.* **4**, 277 (1971).
- [6] J. von Sachs, *Vorlesungen über Pflanzen-physiologie* (W. Engelmann, Leipzig, 1882), Vol. 1, Chap. 36.
- [7] J. von Sachs, *Über Orthotrope und Plagiotrope Pflanzentheile*, Arbeiten des botanischen Instituts in Würzburg Vol. 2 (W. Engelmann, Leipzig, 1879), Chap. 10.
- [8] J. Cook, *Math. Biosci.* **5**, 353 (1969).
- [9] R. Bastien, T. Bohr, B. Moulia, and S. Douady, *Proc. Natl. Acad. Sci. USA* **110**, 755 (2013).
- [10] A. D. Polyanin and V. F. Zaitsev, *Handbook of Nonlinear Partial Differential Equations: Exact Solutions, Methods, and Problems* (Chapman and Hall/CRC, New York, 2003).
- [11] R. Bastien, S. Douady, and B. Moulia, *Front. Plant Sci.* **5**, 136 (2014).
- [12] R. Bastien, S. Douady, and B. Moulia, *PLoS Comput. Biol.* **11**, e1004037 (2015).
- [13] R. Chelakkot and L. Mahadevan, *J. R. Soc. Interface* **14**, 20170001 (2017).
- [14] D. Agostinelli, A. Lucantonio, G. Noselli, and A. DeSimone, *J. Mech. Phys. Solids* **136**, 103702 (2020).
- [15] B. Moulia, E. Badel, R. Bastien, L. Duchemin, and C. Eloy, *New Phytol.* **233**, 2354 (2022).
- [16] G. Vecchiato, T. Hattermann, M. Palladino, F. Tedone, P. Heuret, N. P. Rowe, and P. Marcati, *PLoS Comput. Biol.* **19**, e1011538 (2023).
- [17] A. Porat, M. Rivière, and Y. Meroz, *J. Exp. Bot.* **75**, 620 (2024).
- [18] J. Dumais, *Proc. Natl. Acad. Sci. USA* **110**, 391 (2013).
- [19] W. F. P. Pfeffer, *Pflanzenphysiologie: Ein Handbuch der Lehre vom Stoffwechsel und Kraftwechsel in der Pflanze. Kraftwechsel. II* (W. Engelmann, Leipzig, 1904), Vol. 3.
- [20] D. E. Moulton, T. Lessinnes, and A. Goriely, *J. Mech. Phys. Solids* **61**, 398 (2013).
- [21] A. Goriely, *The Mathematics and Mechanics of Biological Growth*, edited by S. S. Antman, L. Greengard, and P. J. Holmes, Interdisciplinary Applied Mathematics Vol. 45 (Springer-Verlag, New York, 2017).
- [22] U. Kutschera, *Adv. Space Res.* **27**, 851 (2001).
- [23] E. B. Blancaflor and P. H. Masson, *Plant Physiol.* **133**, 1677 (2003).
- [24] M. T. Morita, *Annu. Rev. Plant Biol.* **61**, 705 (2010).
- [25] K. Jonsson, Y. Ma, A.-L. Routier-Kierzkowska, and R. P. Bhalerao, *Nature Plants* **9**, 13 (2023).
- [26] H. Chauvet, B. Moulia, V. Legué, Y. Forterre, and O. Pouliquen, *J. Exp. Bot.* **70**, 1955 (2019).
- [27] N. Levernier, O. Pouliquen, and Y. Forterre, *Front. Plant Sci.* **12**, 651928 (2021).
- [28] O. M. O'Reilly and T. Treserras, *Int. J. Solids Struct.* **48**, 1239 (2011).
- [29] S. Timoshenko, *J. Opt. Soc. Am.* **11**, 233 (1925).
- [30] D. E. Moulton, T. Lessinnes, and A. Goriely, *J. Mech. Phys. Solids* **142**, 104022 (2020).
- [31] O. M. O'Reilly, *Modeling Nonlinear Problems in the Mechanics of Strings and Rods: The Role of the Balance Laws*, Interaction of Mechanics and Mathematics (Springer, Cham, 2017).
- [32] S. Tsugawa, Y. Miyake, K. Okamoto, M. Toyota, H. Yagi, M. Terao Morita, I. Hara-Nishimura, T. Demura, and H. Ueda, *Sci. Rep.* **13**, 11165 (2023).
- [33] See Supplemental Material at <http://link.aps.org/supplemental/10.1103/PhysRevE.110.014405> for movies showing dynamics.
- [34] W. K. Silk and R. O. Erickson, *J. Theor. Biol.* **76**, 481 (1979).
- [35] M. Rivière, Y. Corre, A. Peaucelle, J. Derr, and S. Douady, *J. Exp. Bot.* **71**, 6408 (2020).
- [36] B. Moulia, S. Douady, and O. Hamant, *Science* **372**, eabc6868 (2021).
- [37] Y. Meroz, *New Phytol.* **229**, 1911 (2021).
- [38] M. Rivière and Y. Meroz, *Proc. Natl. Acad. Sci. USA* **120**, e2306655120 (2023).
- [39] H. Levine and D. I. Goldman, *Soft Matter* **19**, 4204 (2023).
- [40] A. Porat, F. Tedone, M. Palladino, P. Marcati, and Y. Meroz, *Front. Robotics AI* **7**, 89 (2020).
- [41] A. Goriely, D. E. Moulton, and L. Angela Mihai, *J. Elast.* **153**, 509 (2023).
- [42] S. S. Antman, *Nonlinear Problems of Elasticity*, 2nd ed., edited by S. S. Antman, J. E. Marsden, and L. Sirovich, Applied Mathematical Sciences Vol. 107 (Springer, New York, 2005).
- [43] M. L. Evans, *Plant Physiol.* **95**, 1 (1991).
- [44] H. Chauvet, O. Pouliquen, Y. Forterre, V. Legué, and B. Moulia, *Sci. Rep.* **6**, 35431 (2016).
- [45] O. Pouliquen, Y. Forterre, A. Béruit, H. Chauvet, F. Bizet, V. Legué, and B. Moulia, *Phys. Biol.* **14**, 035005 (2017).
- [46] N. Hale, Chebyshev polynomials, in *Encyclopedia of Applied and Computational Mathematics*, edited by B. Engquist (Springer, Berlin, 2015) pp. 203–205.
- [47] W. H. Press, S. A. Teukolsky, W. T. Vetterling, and B. P. Flannery, *Numerical Recipes: The Art of Scientific Computing*, 3rd ed. (Cambridge University Press, New York, 2007), Chap. 5.
- [48] A. K. Morris and W. K. Silk, *Bull. Math. Biol.* **54**, 1069 (1992).